JCB Journal of Cell Biology

REPORT

Factors promoting nuclear envelope assembly independent of the canonical ESCRT pathway

I-Ju Lee[1,2], Ema Stokasimov[1,2], Nathaniel Dempsey[1,2], Joseph M. Varberg[3], Etai Jacob[4], Sue L. Jaspersen[3,6], and David Pellman[1,2,5]

The nuclear envelope (NE) undergoes dynamic remodeling to maintain NE integrity, a process involving the inner nuclear membrane protein LEM2 recruiting CHMP7/Cmp7 and then ESCRT-III. However, prior work has hinted at CHMP7/ESCRT-independent mechanisms. To identify such mechanisms, we studied NE assembly in *Schizosaccharomyces japonicus,* a fission yeast that undergoes partial mitotic NE breakdown and reassembly. *S. japonicus* cells lacking Cmp7 have compromised NE sealing after mitosis but are viable. A genetic screen identified mutations that promote NE integrity in *cmp7Δ* cells. Unexpectedly, loss of Lem2 or its interacting partner Nur1 suppressed *cmp7Δ* defects. In the absence of Cmp7, Lem2 formed aggregates that appear to interfere with ESCRT-independent NE sealing. A gain-of-function mutation implicated a membrane and ESCRT-III regulator, Alx1, in this alternate pathway. Additional results suggest a potentially general role for unsaturated fatty acids in NE integrity. These findings establish the existence of mechanisms for NE sealing independent of the canonical ESCRT pathway.

Introduction

In eukaryotes, the nuclear envelope (NE) separates the nucleoplasm and cytoplasm. During cell division, the NE undergoes complex dynamics, necessitating mechanisms for controlled remodeling. In metazoans, the NE is disassembled, partially or completely, at the beginning of mitosis and reassembled after the completion of chromosome segregation. NE remodeling also occurs during interphase nuclear pore complex insertion in all eukaryotes (Grossman et al., 2012; Ungricht and Kutay, 2017) and for spindle pole body (SPB) insertion and/or removal in yeast (Cavanaugh and Jaspersen, 2017; Ding et al., 1997). Finally, pathological "rupture" of the NE, which can then undergo membrane repair, occurs in a variety of circumstances (Halfmann et al., 2019; Hatch and Hetzer, 2014; Shah et al., 2017). Failure to establish or maintain NE integrity compromises genome integrity, as occurs during aging, cellular senescence, cancer, or cell migration through confined spaces (Bakhoum et al., 2018; Spektor et al., 2017; Umbreit and Pellman, 2017; Ungricht and Kutay, 2017). Understanding the mechanisms underlying NE dynamics thus has broad implications for cell and organismal physiology.

Recent studies have suggested that the endosomal sorting complex required for transport (ESCRT) machinery plays a major role in many of the above described aspects of NE dynamics (Frost et al., 2012; Radulovic et al., 2018). ESCRT is best known for mediating scission of membranes that bud away from the cytoplasm (Christ et al., 2017; McCullough et al., 2018; Schöneberg et al., 2017; Scourfield and Martin-Serrano, 2017). Using process-specific cues, the ESCRT-III proteins are recruited to different sites of action and assemble into polymers. The polymers are then remodeled by the ATPases Associated with diverse cellular Activities (AAA ATPase) Vps4 to promote membrane scission. In several cellular processes mediated by ESCRT, ESCRT-III proteins are recruited both by the ESCRT-I/II complexes and/or the Bro1-domain containing protein Alix (Henne et al., 2011; Schöneberg et al., 2017). At the NE, the only known adaptor protein for ESCRT-III recruitment is CHMP7 (Chm7 in budding yeast or Cmp7 in fission yeast; Vietri et al., 2015; Webster et al., 2016; Gu et al., 2017; Pieper et al., 2020), which contains both an ESCRT-II–like domain and an ESCRT-III–like domain (Bauer et al., 2015). CHMP7 itself can be recruited to the NE by a direct physical interaction with the inner nuclear membrane protein LEM2 (Heh1 in budding yeast and Lem2 in fission yeasts; Appen et al., 2019; Pieper et al., 2020). This interaction is normally prevented by spatial separation of CHMP7 and LEM2 because of active export of CHMP7 from the nucleus (Thaller et al., 2019; Vietri et al., 2019). Disruption of

[1]Department of Pediatric Oncology, Dana-Farber Cancer Institute, Boston, MA; [2]Department of Cell Biology, Harvard Medical School, Boston, MA; [3]Stowers Institute for Medical Research, Kansas City, MO; [4]Department of Medical Oncology, Dana-Farber Cancer Institute, Boston, MA; [5]Howard Hughes Medical Institute, Chevy Chase, MD; [6]Department of Molecular and Integrative Physiology, University of Kansas Medical Center, Kansas City, KS.

Correspondence to David Pellman: david_pellman@dfci.harvard.edu; I-Ju Lee: i-ju_lee@dfci.harvard.edu.

© 2020 Lee et al. This article is distributed under the terms of an Attribution–Noncommercial–Share Alike–No Mirror Sites license for the first six months after the publication date (see http://www.rupress.org/terms/). After six months it is available under a Creative Commons License (Attribution–Noncommercial–Share Alike 4.0 International license, as described at https://creativecommons.org/licenses/by-nc-sa/4.0/).

the NE during mitosis or pathological NE rupture enables LEM2 and CHMP7 to form a complex that activates ESCRT-III polymerization, providing one simple regulatory mechanism to control ESCRT activity at the NE. Intriguingly, near-complete RNAi-mediated depletion of LEM2, CHMP7, or ESCRT-III proteins (Olmos et al., 2015; Vietri et al., 2015) resulted in only a partial delay in reestablishing NE integrity after mitosis or rupture. This finding could be explained by incomplete RNAi depletion or by the existence of additional mechanisms that regulate NE dynamics. Supporting the latter possibility, NE repair was also only mildly affected by CHMP7 knockdown, but was abolished when three different LEM (Lap2-Emerin-Man1)-domain proteins were depleted (Halfmann et al., 2019).

Here we use the fission yeast *Schizosaccharomyces japonicus* to study mechanisms for NE assembly after mitosis. *S. japonicus* is an unusual yeast in that it undergoes a semi-open mitosis, where the NE is broken during anaphase with complete but transient loss of NE integrity (Aoki et al., 2011; Yam et al., 2011). After mitosis, the *S. japonicus* NE is reassembled (hereafter "sealing"), a process that requires membrane fusion, as occurs in metazoan cells. In *S. japonicus*, we find an important but nonessential role for Cmp7 and ESCRT-III in NE sealing, which enabled the design of a genetic screen to identify alternative mechanisms. This screen has identified factors that bypass the canonical ESCRT-mediated pathway for NE sealing.

Results and discussion

Normal NE sealing after mitosis in *S. japonicus* requires Cmp7/ESCRT-III

The following findings suggested that the canonical LEM2-CHMP7-ESCRT-III pathway for postmitotic NE reassembly is operative in *S. japonicus*. First, Cmp7 and ESCRT-III localize to putative NE sealing sites. In postmitotic *S. japonicus* cells, NE remodeling is required at the spindle pole after SPB removal and at the mitotic NE "tail" located in the regions of the daughter NE facing the mid-spindle (Ding et al., 1997; Yam et al., 2011). Lem2 and its interacting partner, Nur1, are enriched at both the SPB and the mitotic NE tail (Pieper et al., 2020). Using Nur1 as a marker for NE sealing sites, we found that immediately after anaphase, both Cmp7 and Vps32, the key subunit of the ESCRT-III polymer (Schöneberg et al., 2017; Teis et al., 2008; Wollert et al., 2009), localized to the SPB and the mitotic NE tail (Fig. 1 A). Second, consistent with findings in other organisms (Gu et al., 2017; Webster et al., 2016), the localization of Cmp7 to potential NE sealing sites depends on Lem2 (Fig. 1 B). Interestingly, *S. japonicus* Cmp7 often formed foci in close proximity to the SPB in interphase, a stage when the NE is intact, and this localization also depends on Lem2 (Fig. 1, A and B).

Cmp7 was also required to establish normal nuclear morphology and NE integrity after mitosis, as evidenced by compromised accumulation of an import reporter (GST-GFP-NLS-GFP, referred to as GFP-NLS; Yam et al., 2011) in *cmp7Δ* cells (Fig. 1, C and D). This defect occurred preferentially following postmitotic NE reassembly because premitotic (mononucleated) *cmp7Δ* cells that established NE integrity from a previous cell cycle generally maintained it throughout interphase (Fig. 1 E). NE rupture was never observed when WT cells were imaged for a comparable time interval. Moreover, *vps32Δ* cells exhibited a similar magnitude NE integrity defect as *cmp7Δ* cells, evident from the nuclear/cytoplasmic ratio of GFP-NLS, despite a much stronger growth defect, determined by colony size after ascus dissection (Fig. 1, F and G). Consistent with another recent report (Pieper et al., 2020), these data indicate that Cmp7 is the main adaptor for the ESCRT-dependent NE sealing in *S. japonicus*, as observed in other cell types.

We next asked if *S. japonicus* cells might exhibit a stronger requirement for Cmp7 in stressed conditions. We focused on cold temperature, because of its profound effect on membrane fluidity and its potential to alter membrane and protein dynamics (Ernst et al., 2016). Indeed, *cmp7Δ* cells displayed an aggravated NE integrity defect and failed to form colonies on plates at 19°C (Fig. S1, A and B). *cmp7Δ* cells were also supersensitive to Leptomycin B (LMB; Fig. S1 C), which compromises nucleocytoplasmic transport by inhibiting nuclear export (Kudo et al., 1999; Nishi et al., 1994). LMB sensitivity can be explained by additive effects from defective nucleocytoplasmic transport with partial compromise of NE integrity–like ineffective bailing of a leaky boat.

To characterize NE defects at higher resolution, we performed serial section electron microscopy to compare nuclei from WT and *cmp7Δ* cells grown at 19°C (Fig. 1, H and I). Duplication and insertion of the SPBs in *cmp7Δ* cells was similar to that of WT strains (Fig. S1 D), indicating that Cmp7 is not required for the membrane fusion events that accompany SPB insertion and bipolar spindle formation. However, we frequently observed defects in nuclear shape and structure in *cmp7Δ* cells. The most prominent defect was NE rupture of postmitotic *cmp7Δ* mutant cells that was never observed in WT cells (Fig. 1, H and I; and Fig. S1, E and F). This severe defect of *S. japonicus cmp7Δ* strains contrasts with the near-normal phenotype of *cmp7Δ Schizosaccharomyces pombe* strains (Gu et al., 2017). This likely is explained by the increased need for ESCRT-III to seal the NE in an organism that undergoes mitotic NE disruption. These NE abnormalities have similarities to the defects previously reported for *S. pombe vps4Δ* strains, which include disorganized membranes and some large NE ruptures (Gu et al., 2017). However, *S. japonicus cmp7Δ* strains did not exhibit organized membrane stacks or "karmellae."

Surprisingly, despite the above described defects, *cmp7Δ* cells were viable at 30°C, with 76.9% cells showing nuclear accumulation of GFP-NLS (Figs. 1 F and S2 B). Therefore, although our data indicate an important role for Cmp7/ESCRT-III in the postmitotic NE sealing in *S. japonicus*, they also indicate the existence of one or more Cmp7 and/or ESCRT-III independent NE sealing mechanism(s) under normal growth conditions.

A three-tiered screen for mutations that bypass Cmp7

We designed a genetic screen to identify gene products that function independently of Cmp7 to promote NE sealing. We reasoned that we could most specifically identify parallel pathways by isolating mutations that would bypass a *cmp7* deletion, enhancing the establishment and maintenance of NE integrity in the complete absence of Cmp7. In principle, this approach could

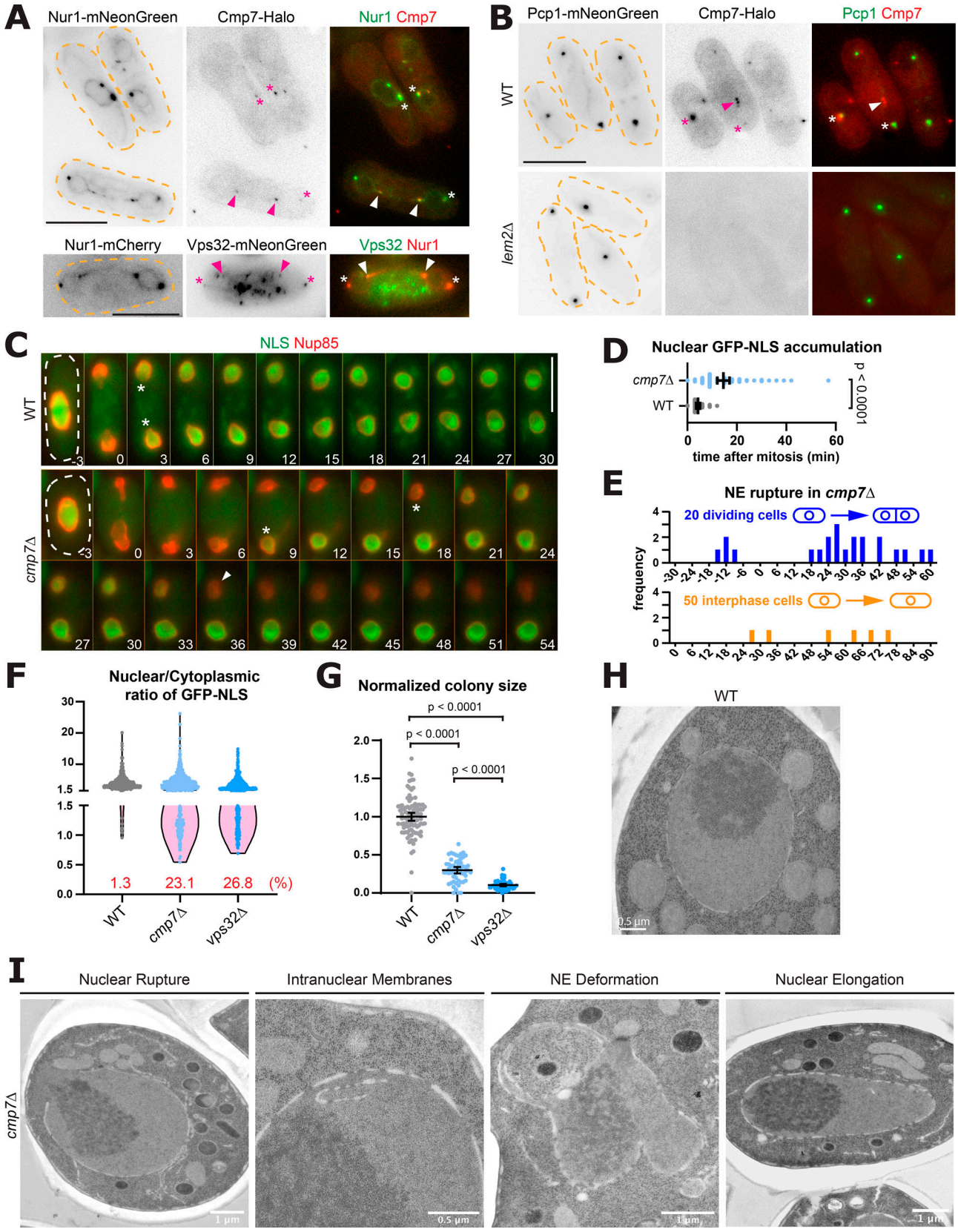

Figure 1. **Cmp7 is required for postmitotic nuclear envelope integrity in *S. japonicus*. (A)** Cmp7 and ESCRT-III localize to sites of NE remodeling. Shown are representative images of *S. japonicus* cells with the indicated fluorescent protein fusions. Asterisks: Cmp7/Vps32 near or at SPBs; arrowheads: Cmp7/Vps32 on postmitotic NE membrane tails. Dashed orange lines: cell border. **(B)** The localization of Cmp7 depends on Lem2. Shown are representative images of WT or *lem2Δ* cells expressing Pcp1-mNeonGreen (SPB) and Cmp7-Halo. **(C)** NE integrity defect of *cmp7Δ* cells. Shown are time lapse series of WT and *cmp7Δ* cells

transiting through mitosis. Time zero is the first time point where two daughter nuclei were evident from the Nup85 signal. Asterisks: first GFP-NLS accumulation in daughter nuclei; arrowhead: an NE rupture event. Scale bars in A–C, 10 µm. **(D)** GFP-NLS appearance in daughter nuclei after mitosis is delayed in *cmp7Δ* cells. *n* = 43 (WT) and 70 (*cmp7Δ*). Means and 95% CI are shown. **(E)** Comparison of the frequency and timing of NE rupture in 20 dividing (top) and 50 interphase (bottom) *cmp7Δ* cells. For interphase cells, time zero was the beginning of the time-lapse movie. NE rupture was defined qualitatively by a decrease in nuclear GFP-NLS. **(F)** *cmp7Δ* and *vps32Δ* both exhibited NE integrity defect. The nuclear/cytoplasmic ratio of GFP-NLS is shown in a violin plot with individual points. Percentage of cells with a ratio lower than 1.5 were shown in red. **(G)** *cmp7Δ* and *vps32Δ* both exhibited growth defect, as assayed by colony size after ascus dissection. Means ± 95% CI are plotted. **(H and I)** Representative EM images of NE morphology in WT (H) and *cmp7Δ* (I) cells. For additional images, see Fig. S1, D and E.

identify gain-of-function mutations in genes that promote Cmp7-independent NE sealing, loss-of-function mutations in negative regulators, or gene products that become toxic in the absence of Cmp7.

A three-tiered screen was performed to identify *cmp7Δ* bypass suppressors (Fig. 2 A). A *cmp7Δ* strain was mutagenized, and fast-growing colonies at 19°C were isolated (Fig. 2 B). After this initial selection, mutant strains were prioritized based on LMB resistance (Fig. 2 C). Finally, we directly assayed the degree of restoration of NE integrity in these mutant strains using fluorescence reporters engineered into the parental strain (Fig. 2 D). We then employed backcrosses, pooled segregant analysis (Birkeland et al., 2010), and whole genome sequencing to identify putative causal suppressor mutations (Table S1). We identified 13 different mutated genes from 33 suppressor strains with a single putative causal mutation. These genes encoded NE proteins as well as proteins not previously implicated in NE remodeling. We introduced several of the mutations into the *cmp7Δ* strain as a definitive test of whether the mutations were responsible for suppression of the defect of *cmp7Δ* cells. Indeed, these mutations were sufficient to enhance the growth of *cmp7Δ* cells at 19°C, albeit with some variable penetrance (Fig. 2 E). Together, these findings validate our approach to identify genes involved in NE sealing after mitosis. Analysis of the most frequently isolated and/or strong phenotype mutations is described below.

Lem2 and Nur1 impair NE sealing in the absence of ESCRT-III

In all organisms examined to date, the localization of CHMP7/Chm7 to sites of NE sealing depends on LEM2/Heh1 (Gu et al., 2017; Webster et al., 2016; Fig. 1 B). It was therefore unexpected that we obtained 11 suppressor strains that carried two different nonsense mutations in *lem2*, both terminating the ORF at the third amino acid. Moreover, we obtained three independent isolates of a missense mutation in Nur1 (Table S1 and Fig. 3 A). Because the *lem2* nonsense mutations we identified were likely to be null alleles, we determined if *lem2Δ* could suppress *cmp7Δ*. Indeed, *lem2Δ* suppressed the growth defect of *cmp7Δ* cells. Strikingly, the deletion of *lem2* also rescued the strong growth defect of *vps32Δ* strains. Deletion of *nur1* also suppressed the growth defects of either *cmp7Δ* or *vps32Δ* strains, albeit less robustly than *lem2Δ* (Fig. 3 B). These findings are difficult to reconcile with the simplest linear model, and suggest additional effects of Lem2 on the maintenance of NE integrity.

One interpretation of these genetic findings is that in the absence of Cmp7, Lem2, and Nur1 become altered in a way that is deleterious to cells. Accordingly, the growth defect of *cmp7Δ* cells was enhanced by a single extra copy of *lem2* expressed from its endogenous promoter, but not by an extra copy of *lem2-m29*, the loss-of-function allele (Fig. 3 C). Interestingly, although an extra copy of WT *nur1* did not significantly affect growth, an extra copy of *nur1-m78* resulted in some suppression of the growth defects (Fig. 3 C), indicating that *nur1-m78* is at least a partially dominant mutation. This can explain why *nur1Δ cmp7Δ* strains exhibited only mild suppression of the *cmp7Δ* growth defect (Fig. 3 B), whereas *nur1-m78 cmp7Δ* strains showed strong suppression (Fig. 2 E).

Next, we addressed the mechanism for the toxicity of Lem2 in strains lacking Cmp7. We noted that in *cmp7Δ* strains, Lem2 localization is significantly altered. In WT cells, Lem2 localizes to the SPB, NE, and the mitotic tail (Yam et al., 2011). Strikingly, in most *cmp7Δ* cells, Lem2 forms one or more aggregates on the NE (Fig. 3 D). As the Lem2–Nur1 complex is known to tether chromatin to the NE (Banday et al., 2016; Barrales et al., 2016; Mekhail et al., 2008), it was recently proposed that unresolved chromatin-NE tethering by these aggregates might generate toxicity because of impaired chromosome segregation (Champion et al., 2019; Chen, 2019; Pieper et al., 2020). We performed a series of experiments to test this idea. First, we examined chromosome segregation in *cmp7Δ* cells by assaying the fluorescence intensity of the kinetochore cluster in anaphase cells (Gregan et al., 2007; Joglekar et al., 2008). We observed an approximately fivefold increase in chromosome segregation errors in *cmp7Δ* cells. However, inconsistent with the model that Lem2 aggregates mediate chromosome mis-segregation, *cmp7Δ lem2Δ* double mutant strains showed an increase, not the predicted decrease, in chromosome mis-segregation relative to *cmp7Δ* single mutants (Fig. 3 E). Additionally, chromosome segregation defects in *S. japonicus* do not produce strong cold sensitivity: strains lacking a monopolin complex component (*mde4Δ*) had a more severe chromosome segregation defect than *cmp7Δ* strains (Choi et al., 2009; Gregan et al., 2007), but *mde4Δ* strains did not exhibit a severe growth defect at 30°C and were only modestly growth-impaired at 19°C (Figs. 3 F and S1 G). Additionally, we did not observe a synergistic growth phenotype in *cmp7Δ mad2Δ* or *vps32Δ mad2Δ* double mutant strains, lacking ESCRT proteins and the spindle assembly checkpoint protein, Mad2 (Fig. 3 G). Finally, *cmp7Δ* strains were not significantly sensitive to thiobendazole (TBZ), which induces chromosome mis-segregation due to impaired microtubule function (Fig. 3 F). In summary, our data suggest that, although Lem2 adversely affects the growth of ESCRT-deficient strains, this growth defect is not primarily due to compromised chromosome segregation.

Alternatively, the "toxicity" of Lem2 in *cmp7Δ* strains could be due to effects on NE integrity. Consistent with results from our initial screen (Fig. 2 D), the NE integrity of *lem2Δ cmp7Δ* and

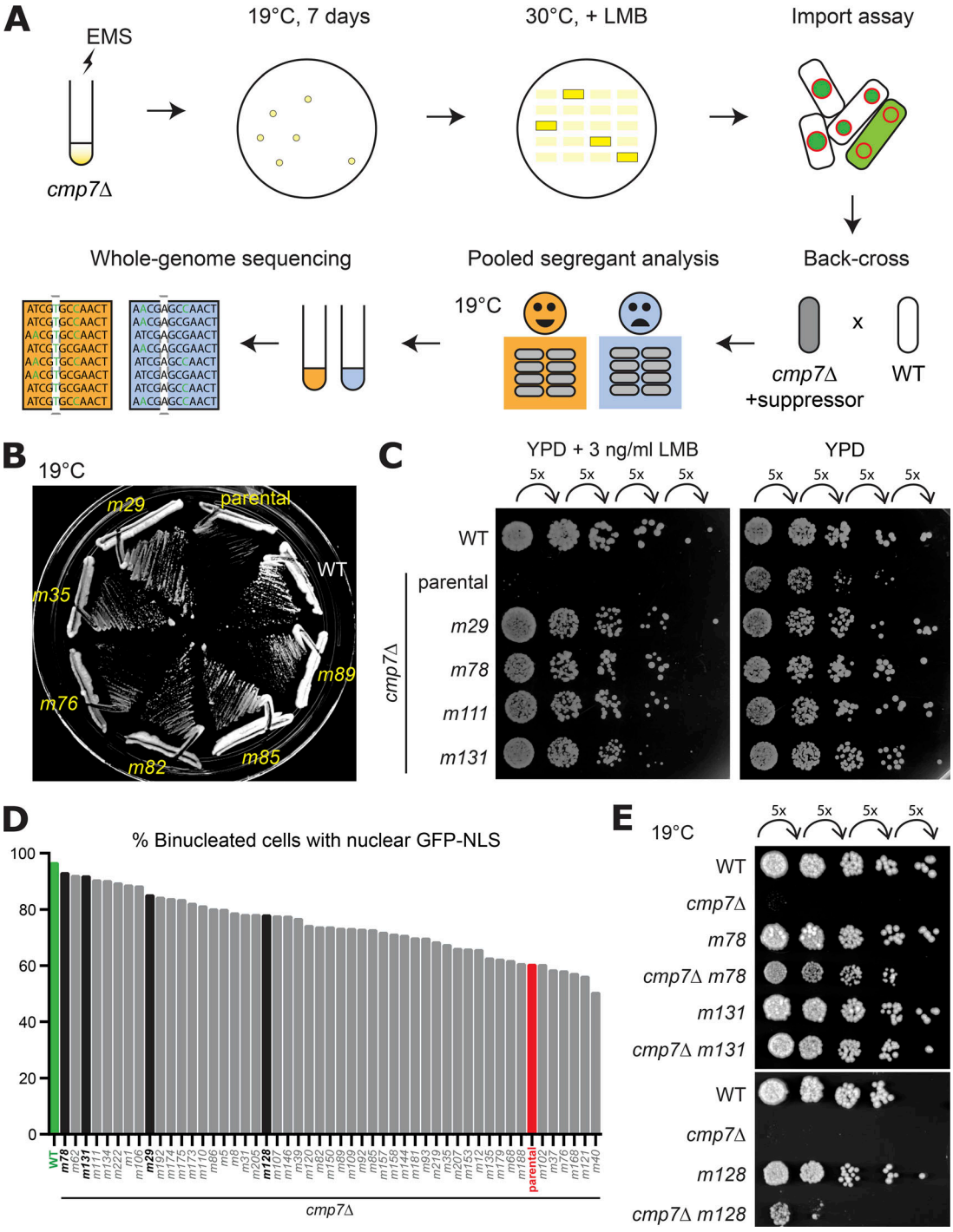

Figure 2. **A three-tiered screen to identify *cmp7Δ* bypass-suppressors with improved NE integrity. (A)** Overview of the screen. **(B)** Growth phenotype of mutant strains. Shown are WT, *cmp7Δ* (parental), and six different suppressor strains grown on YE5S plates at 19°C for 7 d. **(C)** WT, *cmp7Δ*, and four different suppressor strains grown on YPD (right) or YPD with LMB (left) for 3 d at 30°C. **(D)** Suppressors restore NE integrity of *cmp7Δ* strains. Percentage of bi-nucleated cells with nuclear GFP-NLS in both daughter nuclei at 30°C in WT (green), parental *cmp7Δ* (red), and 50 suppressor strains. *n* = 40–291. Mutants described in this study are highlighted. **(E)** Growth of strains engineered with the indicated suppressor mutations grown for 8 d at 19°C.

lem2Δ vps32Δ double mutant strains was significantly improved relative to *cmp7Δ* or *vps32Δ* single mutants. This was apparent by measuring the nuclear/cytoplasmic ratio of GFP-NLS (Fig. 3 H) as well as the time interval for the accumulation of the GFP-NLS reporter in daughter nuclei after mitosis (Fig. 3 I). Thus, our data reveal a surprising inhibitory role for Lem2/Nur1 in postmitotic NE sealing in ESCRT-III mutants, which occurs, at least in part, by interfering with NE integrity. Lem2 aggregates could compromise NE integrity directly or indirectly, by inhibiting ESCRT-independent NE sealing.

The genetic interaction between *lem2Δ* and *cmp7Δ* that we observe in *S. japonicus* contrasts with the genetic interactions

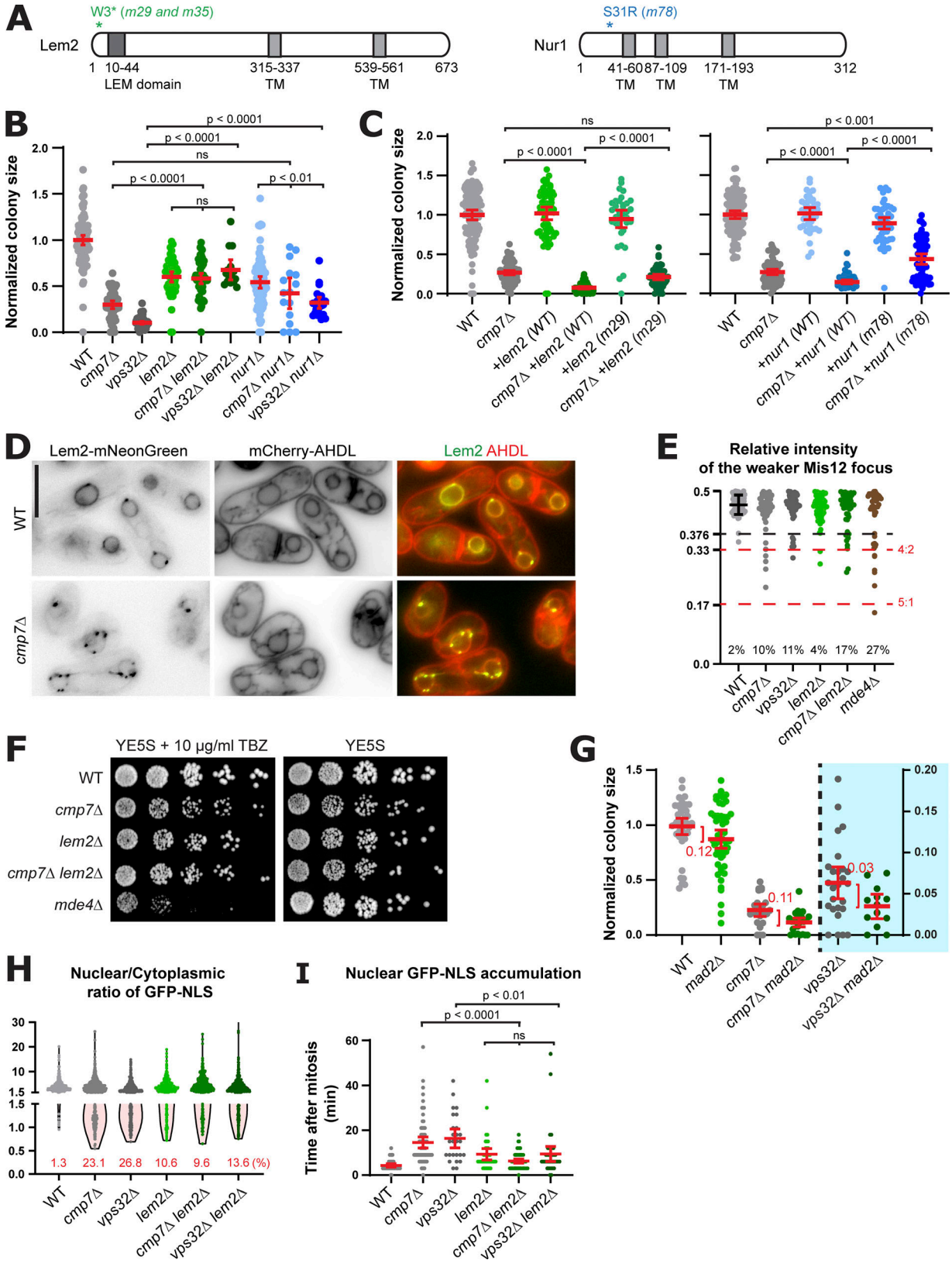

Figure 3. **In the absence of ESCRT-III, Lem2 and Nur1 compromise NE integrity. (A)** Location of mutations relative within Lem2 and Nur1. TM, transmembrane domain. **(B and C)** Normalized colony size of indicated genotypes after ascus dissection. Means ± 95% CI are shown. ns, not significant. **(B)** Deletion of *lem2* or *nur1* suppressed the growth defect of *cmp7/vps32* mutants. **(C)** Effects of an extra copy of *lem2* or *nur1*, WT or the mutant, in suppressing the *cmp7Δ* growth defect. **(D)** Representative images of WT (top) or *cmp7Δ* (bottom) cells expressing Lem2-mNeonGreen and mCherry-AHDL. Scale bar, 10 μm. **(E)** Deletion of *lem2* did not rescue the chromosome segregation defects of *cmp7Δ* cells, as assayed by fluorescent intensity of the kinetochore cluster during

anaphase. See Materials and methods for details. Relative fluorescence intensity of the dimmer kinetochore cluster is plotted. Mean ± SD of the WT cells were shown. Percentages of chromosome mis-segregation (ratio <0.376) in the indicated strains are shown in the plot. Red horizontal dashed lines indicate the expected intensity ratios for mis-segregation of one chromosome (4:2) or two chromosomes (5:1). *n* = 44–66. **(F)** Growth of indicated strains on YE5S (right) and YE5S with TBZ (left) at 30°C for 3 d. *mde4Δ* was used as positive control. **(G)** Additive growth defects of ESCRT-III mutants and *mad2Δ*. Normalized colony size of indicated genotypes after ascus dissection are shown. The difference between mean colony size of *mad2*$^{+}$ and *mad2Δ* strains are indicated by red brackets. Note the difference in the y axis scale for the two groups of mutations separated by the dashed black line. **(H)** Deletion of *lem2* suppressed the NE integrity defect of ESCRT-III mutants. The nuclear/cytoplasmic ratio of GFP-NLS is shown in violin plot with individual points. Percentage of cells with a ratio lower than 1.5 are shown in red. **(I)** GFP-NLS appearance in daughter nuclei after mitosis shows that Lem2 and Nur1 can impair NE reassembly after mitosis in ESCRT-III mutants. *n* = 27–70. Means and 95% CI are shown.

reported in *S. pombe*. In *S. pombe*, loss-of-function mutations in *lem2* or *cmp7* behave similarly, suppressing the pleiotropic defects of cells lacking Vps4, the ATPase that disassembles ESCRT-III filaments (Gu et al., 2017). Consistent with the LEM2–CHMP7–ESCRT-III linear recruitment model (Thaller et al., 2019; Vietri et al., 2019; Webster et al., 2016), this finding was most simply interpreted by Lem2 generating toxicity in an ESCRT-III– and Cmp7-dependent manner. By contrast, in *S. japonicus*, we found that *cmp7Δ* and *lem2Δ* have different phenotypes, displaying an alleviating genetic interaction. Our finding, therefore, identifies an ESCRT-III–independent effect of Lem2 in *S. japonicus*.

An *alx1* mutation that promotes NE sealing in the absence of Cmp7

One mutant, *m131*, results in a Glu to Val substitution at position 308 in the *SJAG_03891* ORF, which encodes one of the two Bro1-domain–containing proteins in *S. japonicus* (Fig. 4 A). The *alx1-m131* mutation is adjacent to the concave ESCRT-III–binding surface, based on the structure of human and budding yeast Bro1 domains (McCullough et al., 2018; Fig. 4 A). Bro1-domain–containing proteins have not previously been implicated in postmitotic NE sealing. We named *SJAG_03891 alx1* and investigated its localization and role in NE integrity.

Both Alx1 and Alx1-m131 localized to SPB and mitotic tails in dividing cells (Fig. 4 B) and are present in cells at similar steady-state levels (Fig. 4 C). Normal localization and protein levels raised the possibility that *alx1-m131* might be a dominant gain-of-function mutation, a category of suppressors expected to be identified in our screen. Indeed, we found that *alx1-m131* suppressed the growth defect of the *cmp7Δ* strain even in the presence of WT *alx1* (Fig. 4 D). We determined if *alx1-m131* suppressed the defect of *cmp7Δ* cells by preventing the formation of the toxic Lem2/Nur1 aggregates. However, the formation of the Lem2/Nur1 aggregates was unaffected in *alx1-m131 cmp7Δ* cells (Fig. 4 B).

Next, we characterized the growth and NE integrity of a *cmp7Δ lem2Δ alx1-m131* strain to that of a control *cmp7Δ lem2Δ* strain. If *alx1-m131* suppression of the *cmp7Δ* defect is explained by disruption of the Lem2 aggregates, it is expected that *alx1-m131 cmp7Δ lem2Δ* and *cmp7Δ lem2Δ* strains would be indistinguishable, as Lem2 toxic aggregation will not occur in either strain. Alternatively, if *alx1-m131* were to promote NE sealing independent of the Lem2 aggregates, *alx1-m131* should promote growth and NE integrity whether or not Lem2 is present in cells. Indeed, we found that *alx1-m131 cmp7Δ lem2Δ* strains showed improved growth and NE integrity relative to *cmp7Δ lem2Δ* strains (Fig. 4, E and F). Together, these data indicate that *alx1-m131* is a dominant gain-of-function mutation that promotes NE integrity independent of Cmp7 and independent of toxic Lem2 aggregates.

The *alx1-m131* mutation could enhance a normal function of Alx1 in maintaining NE integrity, or it could repurpose Alx1 from another ESCRT-regulated process (e.g., a neomorphic mutation). To distinguish these models, we characterized the phenotype of cells lacking Alx1. *alx1Δ* strains had no measurable growth defect but did exhibited a subtle NE-sealing defect. However, *cmp7Δ alx1Δ* strains did exhibit aggravated growth and an aggravated NE integrity defect (Fig. 4, F and G; and Fig. S2 P). Therefore, Alx1 contributes to growth and NE integrity independently of Cmp7, a function that is enhanced by the *alx1-m131* mutation.

We next asked if *alx1-m131* promoted NE sealing by recruiting ESCRT-III to the NE. In *cmp7Δ* cells, both Alx1 and Alx1-m131 colocalized with some of the Nur1 aggregates (Fig. 4 B), but Vps32 was not detected in these foci in either strain (Fig. 4 H). This negative result is not conclusive because it could be due to limited detection sensitivity, given that the Vps32 signal at NE sealing sites is weak (Fig. 1 A). Nevertheless, an alternative interpretation is that *alx1-m131*, at least in part, suppresses the NE integrity defects of *cmp7Δ* cells via an ESCRT-independent mechanism. The possibility the Bro1-domain proteins could have ESCRT-independent effects has been raised in prior studies of these proteins in the context of virus budding (Bardens et al., 2011; Popov et al., 2009). To assess this possibility, we compared the growth of *alx1Δ vps32Δ*, *alx1-m131 vps32Δ*, and *vps32Δ* strains. Surprisingly, *alx1Δ vps32Δ* strains exhibited a stronger growth defect than *vps32Δ* (Fig. 4 I), whereas *alx1-m131* improved the growth of *vps32Δ* cells. These data indicate an ESCRT-independent function of *alx1-m131*. Although the genetic data are most consistent with this function being related to NE sealing, absent more information on the underlying mechanism, we do not exclude effects related to other ESCRT functions.

Overexpression of Ole1 enhances NE sealing after mitosis

In addition to dedicated membrane fusion machineries, such as ESCRT, membrane fusion can be enhanced by altering the biophysical properties of the lipid bilayer (Chernomordik and Kozlov, 2003; Kinugasa et al., 2019; Penfield et al., 2019). Interestingly, our screen identified several mutations in *ole1*, the gene encoding the only Δ9 fatty acid desaturase in *S. japonicus* (Stukey et al., 1989; Makarova et al., 2020). Like its homologues (Tatzer et al., 2002), Ole1 localizes to the ER membrane (Fig. 5 A). Unsaturated acyl chains are poorly packed within lipid

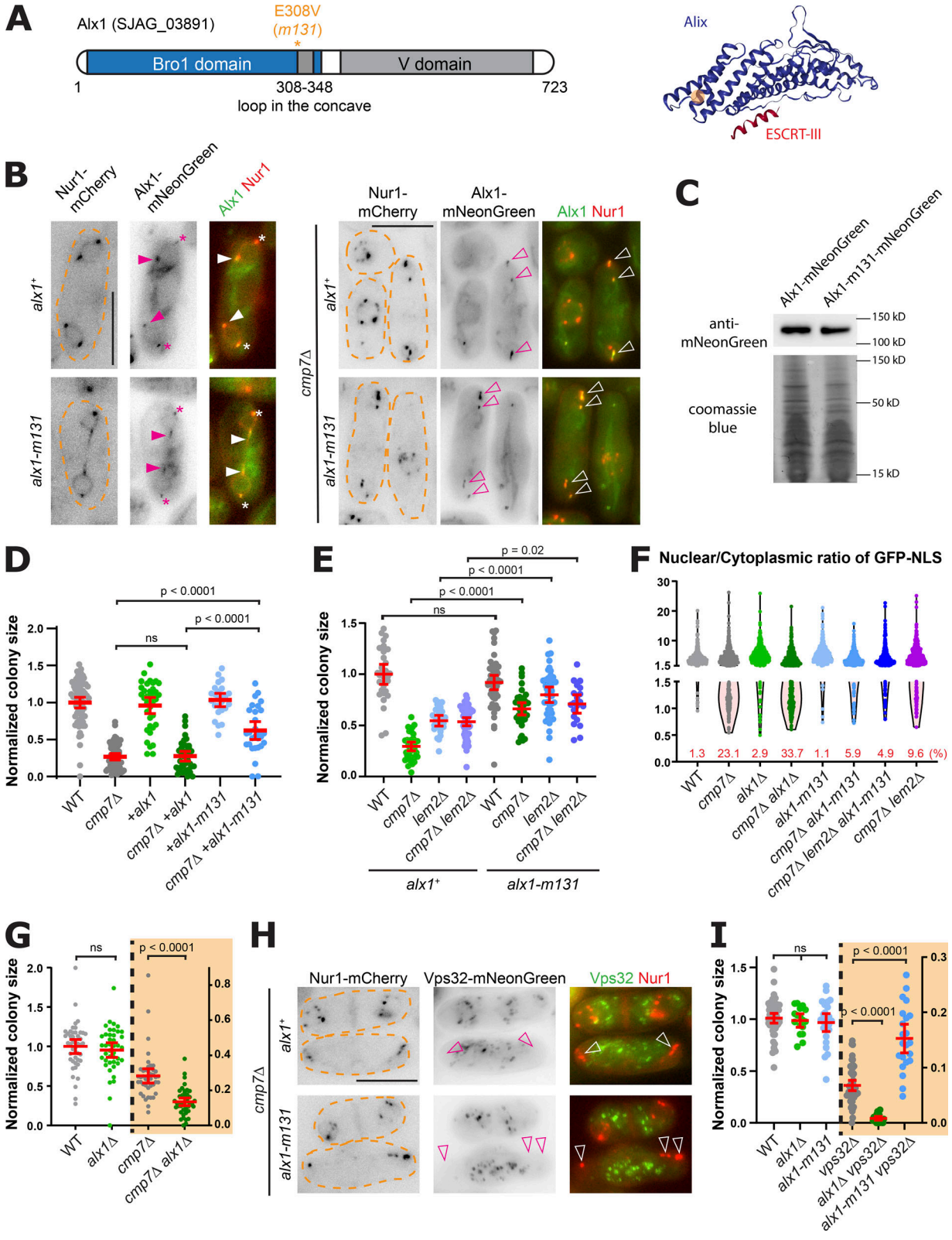

Figure 4. **Alx1 is required for NE integrity. (A)** Position of the *m131* mutation within Alx1's Bro1 domain (left: schematic; right: on the human Alix Bro1 domain structure). In the structure, the Bro1 domain of human Alix is blue and the last helix of CHMP4B/Vps32 is red (adapted from www.rcsb.org/structure/3C3Q). The location of the residue mutated in *m131* is highlighted in orange. **(B)** Localization of Alx1 and Alx1-m131 in WT and *cmp7Δ* cells. Asterisks: Alx1/Alx1-m131 at or adjacent to SPBs; closed arrowheads: Alx1/Alx1-m131 on postmitotic NE membrane tails; open arrowheads, Alx1/Alx1-m131 on Nur1 foci in *cmp7Δ* cells. Dashed lines: cell border. Scale bar, 10 µm. **(C)** Steady-state levels of Alx1 and Alx1-m131 by immunoprecipitation. **(D)** *alx1-m131* is a dominant, gain-of-function mutation for cell growth. **(E)** *alx1-m131* rescues the growth of *cmp7Δ* lem2Δ cells. **(F)** *alx-m131* promotes NE integrity in *cmp7Δ lem2Δ* cells. The nuclear/

cytoplasmic ratio of GFP-NLS is shown in violin plot with individual points. Percentage of cells with a ratio lower than 1.5 are shown in red. **(G)** Consistent with parallel function, *alx1Δ* enhanced the growth defect of *cmp7Δ* cells. **(H)** Localization of Vps32 in *cmp7Δ* and *cmp7Δ alx-m131* strains. Open arrowheads, Nur1 foci in mitotic cells. Scale bar, 10 µm. **(I)** *alx1-m131* enhanced the growth of *vps32Δ* cells, whereas *alx1Δ* exacerbated this growth defect. For panels showing genetic interactions assayed by colony size after dissection (D, E, G, and I), Means ± 95% CI are plotted. ns, not significant. Note the difference in the y axis scale for the two groups of mutations in G and I separated by the dashed black line.

bilayers, which is predicted to increase membrane fluidity (Harayama and Riezman, 2018) in a manner that may promote NE sealing. To determine if increased fatty acid desaturase activity would promote NE sealing in the absence of Cmp7, we overexpressed *ole1* from the medium-strength *Purg1* promoter (Watt et al., 2008). Indeed, *Purg1-ole1* partially suppressed the growth defect of *cmp7Δ* strains (Fig. 5 B). Moreover, overexpression of Ole1 also resulted in a subtle but statistically significant rescue of the NE sealing defect in binucleated *cmp7Δ* cells (Fig. 5 C). Together, these results further support an important contribution of lipid composition for NE sealing in the absence of Cmp7, as was suggested for *S. pombe* cells lacking Lem2 (Kinugasa et al., 2019). Optimal membrane lipid composition might promote the function of membrane fusion proteins or possibly facilitate the spontaneous fusion of tethered membranes.

Summary

Here, we have taken a genetic and cell biological approach to identify factors required for postmitotic NE sealing. *S. japonicus* is an ideal system to address this problem, because it undergoes partial mitotic NE breakdown but retains facile genetics. Our results highlight a key role of ESCRT in NE membrane sealing, but also establish that NE sealing can occur in the absence of ESCRT-III because strains lacking Cmp7 or Vps32 are viable with only partial defects in NE integrity.

In principle, ESCRT-independent NE membrane fusion might be promoted by another dedicated membrane fusion machinery, or more speculatively, by membrane tethering that enables spontaneous membrane fusion (Chernomordik and Kozlov, 2003). Both classes of mechanism would be affected by membrane lipid composition, a conclusion that is supported by the finds on *ole1* described in this study. Previous work in *Xenopus* egg extracts has suggested a requirement for ER SNAREs for NE membrane assembly (Baur et al., 2007; Wang et al., 2013), which could provide a backup mechanism for ESCRT. However, these studies primarily relied on the addition of blocking antibodies or dominant negative constructs, and evidence for a SNARE requirement for NE fusion is currently lacking in other systems. Moreover, we note that our screen did not identify SNARE proteins or their regulators. An alternative to unidentified membrane fusion proteins mediating ESCRT-independent NE sealing, proteins that enrich near the NE sealing site (e.g., Lem2, Nur1, Alx1) could promote membrane tethering to facilitate spontaneous membrane fusion. Although Lem2 was recently shown to undergo a liquid–liquid demixing phase transition that might enhance membrane tethering (Appen et al., 2019), we found that deletion of Lem2 improves rather than compromises

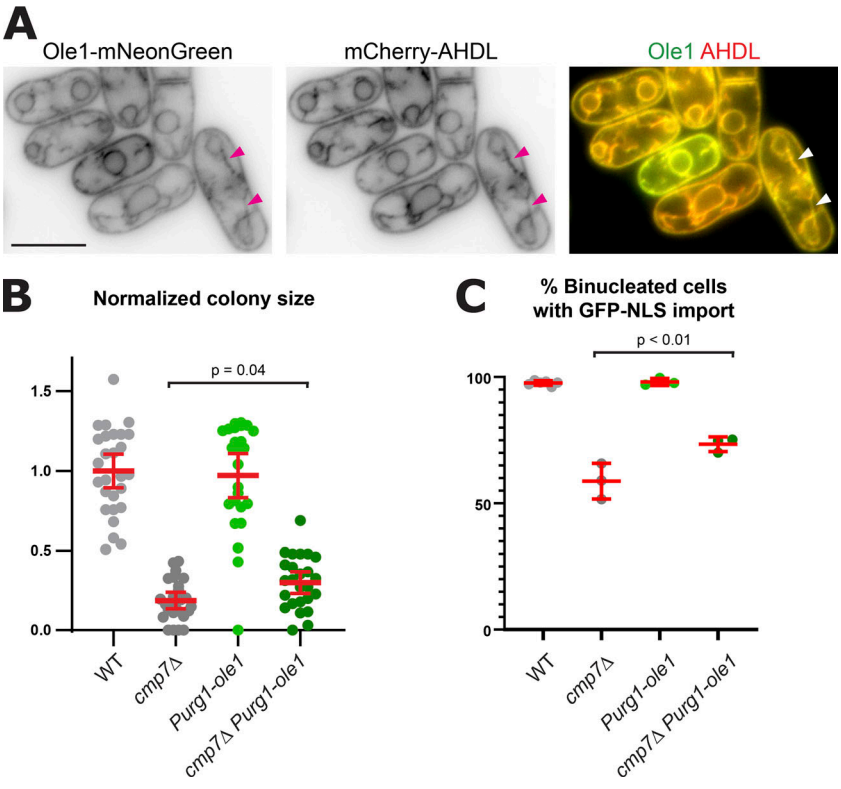

Figure 5. **Overexpression of the fatty acid desaturase Ole1 suppressed the defects of *cmp7Δ* cells. (A)** Ole1 localizes to the ER membrane. Arrowheads, mitotic tails. Scale bar, 10 µm. **(B)** Overexpression of Ole1 partially rescued the growth defect in *cmp7Δ* cells. Means ± 95% CI are plotted. **(C)** Overexpression of Ole1 partially rescued the NE integrity defect in *cmp7Δ* cells. Percentage of binucleated cells with nuclear GFP-NLS in both daughters at 30°C is shown. Mean ± SD from three experiments is shown. *n* = 153–377 per strain in each experiment.

membrane fusion of ESCRT mutants, indicating that Lem2 is not the major ESCRT-III–independent sealing factor. Instead, our results implicate Alx1, and possibly proteins sequestered in Lem2 aggregates, as candidate components of a Cmp7/ESCRT-III–independent NE sealing pathway.

In summary, we present the results of the first unbiased genetic approach to identify factors required for NE sealing. Because common mechanisms may be used for many aspects of NE dynamics, our results may be relevant to other processes such as NE repair after NE disruption (Radulovic et al., 2018).

Materials and methods

S. japonicus strain construction

Transformation of *S. japonicus* cells was performed as described (Aoki et al., 2010), with 2–10 µg purified DNA fragments per transformation. All transformants were verified by PCR at both the 5′ and 3′ insertion junctions. Suppressor mutants created in a WT background were verified by sequencing.

Table S2 lists the *S. japonicus* strains used in this study. DNA fragments for gene targeting and gene deletion were designed as previously described (Bähler et al., 1998) with the exception that 575-bp homologous sequences flanking the designated insertion sites were used for homologous recombination. These homologous sequences were either synthesized as double-stranded gene blocks or PCR-amplified from WT genomic DNA. Fusion to sequences encoding fluorescent proteins and/or selection markers was done by PCR. To introduce extra gene copies, the relevant ORF and 1-kb flanking regulatory sequences were cloned into the plasmid pSJK1 (Aoki et al., 2010) after the *kan* gene using Gibson Assembly. The gene cassette and the *kan* gene were then introduced at the *ura4* locus. To delete *vps32*, a gene that is important for cell growth, *kan-Pvps32-vps32-Tvps32* was integrated into the *ura4* locus before the endogenous *vps32* was deleted. This strain was then crossed to a WT strain to obtain *vps32Δ* cells without *kan-Pvps32-vps32-Tvps32*. To introduce the suppressor mutations *nur1-m78* and *alx1-m131* to their endogenous locus in a WT background, the endogenous *nur1* and *alx1* ORFs were replaced with *Sp-ura4*$^{+}$ (the *ura4*$^{+}$ gene from *S. pombe*; Aoki et al., 2010). A second round of transformation was then to replace *Sp-ura4*$^{+}$ with the mutant *nur1-m78* or *alx1-m131* sequence. 1.5 g/liter 5-fluoroorotic acid in yeast extract with five supplements (YE5S) medium was used for counterselection (Furuya and Niki, 2009).

S. japonicus cell culture and genetic crosses

Cells are grown in YE5S unless otherwise noted. To assay cell growth at different temperatures or with different chemicals, cell cultures in log-phase growth were diluted to the same OD_{600} (0.2–0.4) and serially diluted (fivefold increments) in 96-well plates. To test for sensitivity to microtubule depolymerization, TBZ (Sigma-Aldrich) was added to a final concentration of 10 µl/ml. In a pilot experiment, we found that WT *S. japonicus* was sensitive to LMB at 20 ng/ml in yeast peptone dextrose (YPD). 3 ng/ml LMB was used as a secondary screen for mutations affecting nuclear integrity based on preliminary experiments showing that this concentration of LMB inhibits the growth of *cmp7Δ* strains but not the WT controls.

For crosses, cells of the opposite mating type were mixed on sporulation agar and incubated at 30°C for 12–16 h. Cells were then dissected on a YE5S plate using a yeast dissection microscope (Nikon Instruments, Inc., and Micro Video Instruments, Inc.). Asci were incubated at 32°C for 6–8 h before spores were separated onto different spots. Dissected spores were incubated at 30°C for 3–4 d before further experiments or analysis. A complete *S. japonicus* ascus contains eight spores (Furuya and Niki, 2009). However, a mature ascus that had released one or two spores was almost indistinguishable from a complete ascus under a yeast dissection microscope, making it infeasible to only analyze asci with eight spores. Only asci that had more than six spores after dissection were analyzed in this study.

To analyze colony size after asci dissection, plates containing colonies germinated from spores were scanned, and unbiased colony size analysis was performed using the "Analyze Particles" function in ImageJ/FIJI. Table S2 lists all strains used in the crosses. For each cross, colonies from 14–35 asci were analyzed. Colonies were then restreaked, and their genotypes were identified by replica-plating and/or PCR. For each genotype, colony sizes were normalized to the average size of WT colonies on the same plate. Because of the prominent growth defect of *vps32Δ* cells, we used PY7579 (*vps32Δ::natMX6 ura4-D3::kan-Pvps32-vps32-Tvps32*) in crosses to determine the genetic interactions between *vps32Δ* and deletions of other genes. Only the sizes of colonies that did not have the extra copy of *vps32* at the *ura4* locus were plotted. Colonies carrying *alx1-m131* were identified by Sanger sequencing after ascus dissection.

Microscopy and image analysis

Cells for microscopy were collected from liquid culture in log-phase growth at 28–30°C unless otherwise noted. After centrifugation, cell pellets were washed into the Edinburgh Minimal Medium (EMM) and imaged in 35-mm glass-bottom dishes (MatTek Corporation). For time-lapse videos, cells were imaged in YE5S. For visualization of Cmp7-Halo (Los et al., 2008), the fluorescent dye JF549 (Promega; Grimm et al., 2015) was added to a final concentration of 500 nM 2 h before imaging. Images were collected using a 100×/1.4 NA lens on a Nikon Ti2 Microscope equipped with a Hamamatsu Flash4.0 V2+ sCMOS camera and Lumencor SpectraX fluorescence light source, or a 100×/1.4 NA lens on a DeltaVision microscope (Applied Precision Inc.) equipped with a Photometrics CoolSnap HQ camera. Acquisition software was either NIS-Elements or *DeltaVision* softWoRx. A z-focal plane series was acquired at 0.2–0.4 µm intervals spanning 8 µm. Maximum-intensity projections of five 0.4-µm z-slices or ten 0.2-µm z-slices from the middle of the indicated cells are shown unless otherwise noted. Image analysis and preparation were performed using ImageJ/FIJI. Figures were assembled using Adobe Illustrator.

The percent binucleated cells with nuclear GFP-NLS in both daughter nuclei was determined qualitatively. For Fig. 5 C, because of the effect size, the samples were scored double-blind. To determine chromosome mis-segregation rate, strains expressing Mis12-mCherry (kinetochore) GFP-Atb2 (tubulin) were

imaged. The fluorescent intensity of the Mis12 cluster in each z-slice was measured and corrected for cellular background as previously described (Wu et al., 2008). The sum intensity was then calculated for each cluster. Chromosome mis-segregation was defined by having a cluster with a relative fluorescent intensity that was lower than 0.376, which was three SDs from the average in WT cells. To minimize the contribution from photobleaching during z-stack acquisition, only cells with two clusters close to the same focal plane (separated by <2.0 µm in the z-axis) were analyzed.

Single z-slices at the middle of the cells in the field were used to measure the nuclear/cytoplasmic ratio of GFP-NLS (Webster et al., 2016). For each cell, the nuclear and cytoplasmic intensity of GFP-NLS in a region of interest with an area of ∼1 µm^2 were measured. The ratio was calculated after background subtraction. 507–553 cells were measured for each strain.

EM

WT and *cmp7Δ* cells were grown in YE5S media in a 19°C shaking water bath for 72 h. Cells were back-diluted every 24 h to maintain an OD_{600} below 1.0 and harvested during logarithmic phase growth by vacuum filtration onto 0.45 µm Millipore filters. The cells were then frozen in a Leica EM-ICE high-pressure freezer at ∼2,050 bar, then transferred to the Leica EM AFS2 for freeze substitution under liquid nitrogen into 2% osmium tetroxide/0.2% uranyl acetate/5% water/acetone. We used the following procedure for freeze substitution: −90°C to −80°C over 60 h, −80°C to −60°C over 5 h, −60°C for 4 h, −60°C to −20°C over 8 h, held at −20°C for 4 h, and −20°C to 0°C over 5 h, and finally samples were held at 0°C for 3 h. Samples were then removed from the AFS and brought to room temperature. Samples went through four changes of acetone over 1 h and were removed from the planchettes. They were embedded in acetone/Spurr's mixtures to a final concentration of 100% Spurr's over several days in a stepwise procedure as previously described (McDonald, 1999). 60–80-nm serial thin sections were cut on a Leica UC6 ultramicrotome, stained with 4% uranyl acetate and Sato's lead, and imaged on a Zeiss Merlin scanning electron microscope equipped with a scanning transmission electron microscope detector and Atlas software at a pixel size of 20 nm. Additional higher resolution SEM images were acquired at a pixel size of 6 nm, and images of select SPBs and nuclei were acquired on a FEI Tecnai Spirit transmission electron microscope. Original data underlying this manuscript can be accessed from the Stowers Original Data Repository at http://www.stowers.org/research/publications/libpb-1516.

Mutagenesis and bypass suppressor screen

The protocol for mutagenesis of *S. japonicus* was modified from a protocol for *S. pombe* (Ekwall and Thon, 2017). 10^8 PY7509 (*cmp7Δ::kanMX6 GFP-NLS-ura4$^+$ Nup85-mCherry-ura4$^+$*) cells from a log-phase YE5S culture were washed into EMM and incubated with 2% ethyl methanesulfonate for 2 h at room temperature, giving ∼50% survival. The culture was then washed into 5% sterile sodium thiosulfate to quench the activity of ethyl methanesulfonate, and then washed three more times in EMM. Mutagenized cells were then plated onto YE5S plates with a density of 10^5 cells per plate, and then incubated at 19°C for 9 d. 470 large colonies were selected, restreaked for single colonies, and replica plated onto YPD plates with 3 ng/ml LMB to test their growth at 30°C. The top 50 strains that showed significantly improved growth in the presence of LMB compared with the parent strain were selected for further experiments, including imaging to determine the percent of binucleated cells with nuclear GFP-NLS.

Backcrosses to a WT strain (*h$^+$ GFP-NLS-ura4$^+$ nup85-mCherry-ura4$^+$*) were used to identify candidates where suppression resulted from mutation of a single genetic locus. 47 out of 50 crosses gave rise to *cmp7Δ* colonies that grew at 19°C.

Pooled-segregant analysis and whole genome sequencing

To identify putative causal mutations, we performed pooled-segregant analysis followed by whole genome sequencing (Birkeland et al., 2010). After backcrossing, *cmp7Δ* spores with improved growth at 19°C were categorized as suppressed (S), and *cmp7Δ* progenies that were cold sensitive were categorized as non-suppressed (N). 8–12 colonies, each from a different ascus, were selected for each category to ensure statistical power (Abe et al., 2012; Iida et al., 2014). To achieve near-equal representation of each colony, spores were grown separately in 96-well deep-well plates for 12–16 h at 30°C before being combined equally based on OD_{600} measurements. Genomic DNA was extracted from each pool using MasterPure yeast DNA extraction kit (Illumina) with RNase treatment at 37°C overnight. Any residual small nucleotides were removed by AMPure XP beads (Beckman Coulter). The quality of genomic DNA was examined using Genomic DNA Screen Tape on a TapeStation 2200 (Agilent Technologies). Sequencing libraries were made using a plexWell kit (seqWell, Inc.), and the quality of the libraries was determined by Bioanalyzer (Agilent Technologies).

A total of 96 libraries (47 pairs of S and N pools, plus WT and *cmp7Δ* parental cells) were sequenced using NextSeq (paired end 75 × 2), producing on average 10 million reads per sample. Sequencing reads were aligned to the *S. japonicus* reference genome (GCA_000149845.2, release 35) using bwa (https://github.com/lh3/bwa, version bwa-0.7.13) in the paired-end mode by "bwa mem." For all libraries, 94% of the reference genome was covered by at least one read. Before variant discovery was performed, duplicated sequencing fragments were removed by "MarkDuplicates" using the PICARD software suite, and realigning was performed around genomic regions of indels using The Genome Analysis Toolkit (v3.7-0-gcfedb67). Variants for each of the 96 samples were discovered using "HaplotypeCaller" method in Genomic Variant Call Format mode and merged using "GenotypeGVCFs." Variants were annotated using SnpSift version 4.3s (Cingolani et al., 2012) using the annotation of *S. japonicus* (downloaded on October 25, 2017 using snpEff download method). All variants with at least one supporting read were collected and summarized in a table for each pair of S and N strains. SNPs that had 100% penetrance in the S pool (at least 14 reads) and 0% in the N pool of the same mutant (at least 3 reads) were identified as putative causal mutations. Out of 47 suppressors sequenced using the above method, 33 of them contained one putative causal mutation. Several mutations

including *lem2-m29* and *nur1-m78* were isolated multiple times from the screen. Given that we identified different background SNPs in different isolates with the same putative causal mutation, these mutations almost certainly arose multiple times, independently, rather than being the consequence of cell proliferation during mutagenesis.

Immunoprecipitation and immunoblotting

Cells with an OD_{600} below 1.0 were harvested and snap frozen for protein analysis. For each strain, 1 g of cell pellet was pulverized with a mortar and pestle in liquid nitrogen. The frozen powder was resuspended in lysis buffer (10 mM Hepes, pH 7.4, 200 mM NaCl, 3 mM $MgCl_2$, 300 mM sucrose, 1 mM EDTA, 1% Triton X-100, 1 mM DTT, and freshly added PMSF and complete protease inhibitor tablet [Roche]). After centrifugation at 2,000 *g* for 10 min, the lysate was incubated with mNeonGreen trap magnetic beads (Chromotek) at 4°C for 1 h. After a 3× wash, bound proteins were released with sample buffer. The samples were then loaded for SDS-PAGE and Western blotting. Anti-mNeonGreen antibody (32F6, Chromotek) was used at 1:1,000 dilution. Anti-mouse IgG (Sigma-Aldrich) was used at 1:20,000 dilution. Blots were reacted with SuperSignal West Femto Maximum Sensitivity Substrate (Thermo Fisher Scientific) and imaged by a ChemiDoc Imager (BioRad). Lysates were stained with Coomassie blue to assess input protein concentration.

Statistical analysis

Plots were generated using GraphPad Prism. Comparisons of colony size were made using Brown–Forsythe and Welch ANOVA to account for different variances of strains, followed by Tukey's multiple comparison test. Other comparisons were made using one-way ANOVA followed by Tukey's multiple comparison test.

Online supplemental material

Fig. S1 shows the accentuation of the nuclear envelope integrity defect of *cmp7Δ* cells at 19°C. Fig. S2 shows representative images of various mutants expressing GFP-NLS Nup85-mCherry cultured at 30°C. Table S1 lists bypass suppressors of *cmp7Δ* identified in this study. Table S2 lists *S. japonicus* strains used in this study.

Acknowledgments

The authors would like to thank S. Oliferenko (The Francis Crick Institute, London, UK), J.-Q. Wu (The Ohio State University, Columbus, OH), and JapoNet (National Institute of Genetics, Shizuoka, Japan) for reagents, and the Nikon Imaging Center at Harvard Medical School, Center for Cancer Computational Biology at Dana-Farber Cancer Institute, and Melainia McClain in the Electron Microscopy Core at the Stowers Institute for technical support. We thank L.-L. Du, D. Moazed, S. Oliferenko, T. Rapoport, N. Rhind, and members of the Pellman laboratory for discussion.

I-J. Lee was supported by Leukemia and Lymphoma Society Postdoctoral Fellowship 5436-16. The Jaspersen laboratory is supported by the Stowers Institute for Medical Research and by R01GM121443. D. Pellman is a Howard Hughes Medical Institute investigator, and this work was supported by 5R37 GM061345-14.

The authors declare no competing financial interests.

Author contributions: I-J. Lee and D. Pellman conceptualized and designed the experiments. I-J. Lee, E. Stokasimov, and N. Dempsey performed the experiments. I-J. Lee and E. Stokasimov carried out the bypass suppressor screen. I-J. Lee and N. Dempsey analyzed microscopy data. I-J. Lee performed crosses, dissections, and colony size analysis. J.M. Varberg and S.L. Jaspersen performed and analyzed EM. E. Jacob analyzed whole-genome sequencing data. I-J. Lee and D. Pellman wrote the manuscript with input from all co-authors.

Submitted: 30 August 2019
Revised: 11 January 2020
Accepted: 3 March 2020

References

Abe, A., S. Kosugi, K. Yoshida, S. Natsume, H. Takagi, H. Kanzaki, H. Matsumura, K. Yoshida, C. Mitsuoka, M. Tamiru, et al. 2012. Genome sequencing reveals agronomically important loci in rice using MutMap. *Nat. Biotechnol.* 30:174–178. https://doi.org/10.1038/nbt.2095

Aoki, K., R. Nakajima, K. Furuya, and H. Niki. 2010. Novel episomal vectors and a highly efficient transformation procedure for the fission yeast Schizosaccharomyces japonicus. *Yeast.* 27:1049–1060. https://doi.org/10.1002/yea.1815

Aoki, K., H. Hayashi, K. Furuya, M. Sato, T. Takagi, M. Osumi, A. Kimura, and H. Niki. 2011. Breakage of the nuclear envelope by an extending mitotic nucleus occurs during anaphase in Schizosaccharomyces japonicus. *Genes Cells.* 16:911–926. https://doi.org/10.1111/j.1365-2443.2011.01540.x

Appen, A., D. LaJoie, I.E. Johnson, M. Trnka, S.M. Pick, A.L. Burlingame, K.S. Ullman, and A. Frost. 2019. A role for liquid-liquid phase separation in ESCRT-mediated nuclear envelope reformation. *bioRxiv.* 577460.

Bähler, J., J.Q. Wu, M.S. Longtine, N.G. Shah, A. McKenzie III, A.B. Steever, A. Wach, P. Philippsen, and J.R. Pringle. 1998. Heterologous modules for efficient and versatile PCR-based gene targeting in Schizosaccharomyces pombe. *Yeast.* 14:943–951. https://doi.org/10.1002/(SICI)1097-0061(199807)14:10<943::AID-YEA292>3.0.CO;2-Y

Bakhoum, S.F., B. Ngo, A.M. Laughney, J.A. Cavallo, C.J. Murphy, P. Ly, P. Shah, R.K. Sriram, T.B.K. Watkins, N.K. Taunk, et al. 2018. Chromosomal instability drives metastasis through a cytosolic DNA response. *Nature.* 553:467–472. https://doi.org/10.1038/nature25432

Banday, S., Z. Farooq, R. Rashid, E. Abdullah, and M. Altaf. 2016. Role of Inner Nuclear Membrane Protein Complex Lem2-Nur1 in Heterochromatic Gene Silencing. *J. Biol. Chem.* 291:20021–20029. https://doi.org/10.1074/jbc.M116.743211

Bardens, A., T. Döring, J. Stieler, and R. Prange. 2011. Alix regulates egress of hepatitis B virus naked capsid particles in an ESCRT-independent manner. *Cell. Microbiol.* 13:602–619. https://doi.org/10.1111/j.1462-5822.2010.01557.x

Barrales, R.R., M. Forn, P.R. Georgescu, Z. Sarkadi, and S. Braun. 2016. Control of heterochromatin localization and silencing by the nuclear membrane protein Lem2. *Genes Dev.* 30:133–148.

Bauer, I., T. Brune, R. Preiss, and R. Kölling. 2015. Evidence for a Non-endosomal Function of the Saccharomyces cerevisiae ESCRT-III-Like Protein Chm7. *Genetics.* 201:1439–1452. https://doi.org/10.1534/genetics.115.178939

Baur, T., K. Ramadan, A. Schlundt, J. Kartenbeck, and H.H. Meyer. 2007. NSF- and SNARE-mediated membrane fusion is required for nuclear envelope formation and completion of nuclear pore complex assembly in Xenopus laevis egg extracts. *J. Cell Sci.* 120:2895–2903. https://doi.org/10.1242/jcs.010181

Birkeland, S.R., N. Jin, A.C. Ozdemir, R.H. Lyons Jr., L.S. Weisman, and T.E. Wilson. 2010. Discovery of mutations in Saccharomyces cerevisiae by pooled linkage analysis and whole-genome sequencing. *Genetics.* 186:1127–1137. https://doi.org/10.1534/genetics.110.123232

Cavanaugh, A.M., and S.L. Jaspersen. 2017. Big Lessons from Little Yeast: Budding and Fission Yeast Centrosome Structure, Duplication, and Function. *Annu. Rev. Genet.* 51:361–383. https://doi.org/10.1146/annurev-genet-120116-024733

Champion, L., S. Pawar, N. Luithle, R. Ungricht, and U. Kutay. 2019. Dissociation of membrane-chromatin contacts is required for proper chromosome segregation in mitosis. *Mol. Biol. Cell.* 30:427–440. https://doi.org/10.1091/mbc.E18-10-0609

Chen, R.H. 2019. Chromosome detachment from the nuclear envelope is required for genomic stability in closed mitosis. *Mol. Biol. Cell.* 30:1578–1586. https://doi.org/10.1091/mbc.E19-02-0098

Chernomordik, L.V., and M.M. Kozlov. 2003. Protein-lipid interplay in fusion and fission of biological membranes. *Annu. Rev. Biochem.* 72:175–207. https://doi.org/10.1146/annurev.biochem.72.121801.161504

Choi, S.H., M.P. Péli-Gulli, I. Mcleod, A. Sarkeshik, J.R. Yates III, V. Simanis, and D. McCollum. 2009. Phosphorylation state defines discrete roles for monopolin in chromosome attachment and spindle elongation. *Curr. Biol.* 19:985–995. https://doi.org/10.1016/j.cub.2009.05.042

Christ, L., C. Raiborg, E.M. Wenzel, C. Campsteijn, and H. Stenmark. 2017. Cellular Functions and Molecular Mechanisms of the ESCRT Membrane-Scission Machinery. *Trends Biochem. Sci.* 42:42–56. https://doi.org/10.1016/j.tibs.2016.08.016

Cingolani, P., A. Platts, L.L. Wang, M. Coon, T. Nguyen, L. Wang, S.J. Land, X. Lu, and D.M. Ruden. 2012. A program for annotating and predicting the effects of single nucleotide polymorphisms, SnpEff. *Fly.* 6(2):80–92. https://doi.org/10.4161/fly.19695

Ding, R., R.R. West, D.M. Morphew, B.R. Oakley, and J.R. McIntosh. 1997. The spindle pole body of Schizosaccharomyces pombe enters and leaves the nuclear envelope as the cell cycle proceeds. *Mol. Biol. Cell.* 8:1461–1479. https://doi.org/10.1091/mbc.8.8.1461

Ekwall, K., and G. Thon. 2017. Ethyl Methanesulfonate Mutagenesis in Schizosaccharomyces pombe. *Cold Spring Harb. Protoc.* 2017:pdb prot091736.

Ernst, R., C.S. Ejsing, and B. Antonny. 2016. Homeoviscous Adaptation and the Regulation of Membrane Lipids. *J. Mol. Biol.* 428(24, 24 Pt A):4776–4791. https://doi.org/10.1016/j.jmb.2016.08.013

Frost, A., M.G. Elgort, O. Brandman, C. Ives, S.R. Collins, L. Miller-Vedam, J. Weibezahn, M.Y. Hein, I. Poser, M. Mann, et al. 2012. Functional repurposing revealed by comparing S. pombe and S. cerevisiae genetic interactions. *Cell.* 149:1339–1352. https://doi.org/10.1016/j.cell.2012.04.028

Furuya, K., and H. Niki. 2009. Isolation of heterothallic haploid and auxotrophic mutants of Schizosaccharomyces japonicus. *Yeast.* 26:221–233. https://doi.org/10.1002/yea.1662

Gregan, J., C.G. Riedel, A.L. Pidoux, Y. Katou, C. Rumpf, A. Schleiffer, S.E. Kearsey, K. Shirahige, R.C. Allshire, and K. Nasmyth. 2007. The kinetochore proteins Pcs1 and Mde4 and heterochromatin are required to prevent merotelic orientation. *Curr. Biol.* 17:1190–1200. https://doi.org/10.1016/j.cub.2007.06.044

Grimm, J.B., B.P. English, J. Chen, J.P. Slaughter, Z. Zhang, A. Revyakin, R. Patel, J.J. Macklin, D. Normanno, R.H. Singer, et al. 2015. A general method to improve fluorophores for live-cell and single-molecule microscopy. *Nat. Methods.* 12:244–250.

Grossman, E., O. Medalia, and M. Zwerger. 2012. Functional architecture of the nuclear pore complex. *Annu. Rev. Biophys.* 41:557–584. https://doi.org/10.1146/annurev-biophys-050511-102328

Gu, M., D. LaJoie, O.S. Chen, A. von Appen, M.S. Ladinsky, M.J. Redd, L. Nikolova, P.J. Bjorkman, W.I. Sundquist, K.S. Ullman, and A. Frost. 2017. LEM2 recruits CHMP7 for ESCRT-mediated nuclear envelope closure in fission yeast and human cells. *Proc. Natl. Acad. Sci. USA.* 114:E2166–E2175. https://doi.org/10.1073/pnas.1613916114

Halfmann, C.T., R.M. Sears, A. Katiyar, B.W. Busselman, L.K. Aman, Q. Zhang, C.S. O'Bryan, T.E. Angelini, T.P. Lele, and K.J. Roux. 2019. Repair of nuclear ruptures requires barrier-to-autointegration factor. *J. Cell Biol.* 218:2136–2149. https://doi.org/10.1083/jcb.201901116

Harayama, T., and H. Riezman. 2018. Understanding the diversity of membrane lipid composition. *Nat. Rev. Mol. Cell Biol.* 19:281–296. https://doi.org/10.1038/nrm.2017.138

Hatch, E., and M. Hetzer. 2014. Breaching the nuclear envelope in development and disease. *J. Cell Biol.* 205:133–141. https://doi.org/10.1083/jcb.201402003

Henne, W.M., N.J. Buchkovich, and S.D. Emr. 2011. The ESCRT pathway. *Dev. Cell.* 21:77–91. https://doi.org/10.1016/j.devcel.2011.05.015

Iida, N., F. Yamao, Y. Nakamura, and T. Iida. 2014. Mudi, a web tool for identifying mutations by bioinformatics analysis of whole-genome sequence. *Genes Cells.* 19:517–527. https://doi.org/10.1111/gtc.12151

Joglekar, A.P., D. Bouck, K. Finley, X. Liu, Y. Wan, J. Berman, X. He, E.D. Salmon, and K.S. Bloom. 2008. Molecular architecture of the kinetochore-microtubule attachment site is conserved between point and regional centromeres. *J. Cell Biol.* 181:587–594. https://doi.org/10.1083/jcb.200803027

Kinugasa, Y., Y. Hirano, M. Sawai, Y. Ohno, T. Shindo, H. Asakawa, Y. Chikashige, S. Shibata, A. Kihara, T. Haraguchi, and Y. Hiraoka. 2019. The very-long-chain fatty acid elongase Elo2 rescues lethal defects associated with loss of the nuclear barrier function in fission yeast cells. *J. Cell Sci.* 132:jcs229021. https://doi.org/10.1242/jcs.229021

Kudo, N., N. Matsumori, H. Taoka, D. Fujiwara, E.P. Schreiner, B. Wolff, M. Yoshida, and S. Horinouchi. 1999. Leptomycin B inactivates CRM1/exportin 1 by covalent modification at a cysteine residue in the central conserved region. *Proc. Natl. Acad. Sci. USA.* 96:9112–9117. https://doi.org/10.1073/pnas.96.16.9112

Los, G.V., L.P. Encell, M.G. McDougall, D.D. Hartzell, N. Karassina, C. Zimprich, M.G. Wood, R. Learish, R.F. Ohana, M. Urh, et al. 2008. HaloTag: a novel protein labeling technology for cell imaging and protein analysis. *ACS Chem. Biol.* 3:373–382. https://doi.org/10.1021/cb800025k

Makarova, M., M. Peter, G. Balogh, A. Glatz, J.I. MacRae, N.L. Mora, P. Booth, E. Makeyev, L. Vigh, and S. Oliferenko. 2020. Delineating the rules for structural adaptation of membrane-associated proteins to evolutionary changes in membrane lipidome. *Curr Biol.* 30(3):367–380. https://doi.org/10.1016/j.cub.2019.11.043

McCullough, J., A. Frost, and W.I. Sundquist. 2018. Structures, Functions, and Dynamics of ESCRT-III/Vps4 Membrane Remodeling and Fission Complexes. *Annu. Rev. Cell Dev. Biol.* 34:85–109. https://doi.org/10.1146/annurev-cellbio-100616-060600

McDonald, K. 1999. High-pressure freezing for preservation of high resolution fine structure and antigenicity for immunolabeling. *Methods Mol. Biol.* 117:77–97.

Mekhail, K., J. Seebacher, S.P. Gygi, and D. Moazed. 2008. Role for perinuclear chromosome tethering in maintenance of genome stability. *Nature.* 456:667–670. https://doi.org/10.1038/nature07460

Nishi, K., M. Yoshida, D. Fujiwara, M. Nishikawa, S. Horinouchi, and T. Beppu. 1994. Leptomycin B targets a regulatory cascade of crm1, a fission yeast nuclear protein, involved in control of higher order chromosome structure and gene expression. *J. Biol. Chem.* 269:6320–6324.

Olmos, Y., L. Hodgson, J. Mantell, P. Verkade, and J.G. Carlton. 2015. ESCRT-III controls nuclear envelope reformation. *Nature.* 522:236–239. https://doi.org/10.1038/nature14503

Penfield, L., R. Shankar, E. Szentgyörgyi, A. Laffitte, M. Mauro, A. Audhya, T. Müller-Reichert, and S. Bahmanyar. 2019. Local regulation of lipid synthesis controls ER sheet insertion into nuclear envelope holes to complete nuclear closure. *bioRxiv.* 757013.

Pieper, G.H., S. Sprenger, D. Teis, and S. Oliferenko. 2020. ESCRT-III/Vps4 controls heterochromatin-nuclear envelope attachments. *Dev. Cell.* In press. https://doi.org/10.1016/j.devcel.2020.01.028.

Popov, S., E. Popova, M. Inoue, and H.G. Göttlinger. 2009. Divergent Bro1 domains share the capacity to bind human immunodeficiency virus type 1 nucleocapsid and to enhance virus-like particle production. *J. Virol.* 83:7185–7193. https://doi.org/10.1128/JVI.00198-09

Radulovic, M., K.O. Schink, E.M. Wenzel, V. Nähse, A. Bongiovanni, F. Lafont, and H. Stenmark. 2018. ESCRT-mediated lysosome repair precedes lysophagy and promotes cell survival. *EMBO J.* 37:e99753. https://doi.org/10.15252/embj.201899753

Schöneberg, J., I.H. Lee, J.H. Iwasa, and J.H. Hurley. 2017. Reverse-topology membrane scission by the ESCRT proteins. *Nat. Rev. Mol. Cell Biol.* 18:5–17. https://doi.org/10.1038/nrm.2016.121

Scourfield, E.J., and J. Martin-Serrano. 2017. Growing functions of the ESCRT machinery in cell biology and viral replication. *Biochem. Soc. Trans.* 45:613–634. https://doi.org/10.1042/BST20160479

Shah, P., K. Wolf, and J. Lammerding. 2017. Bursting the Bubble - Nuclear Envelope Rupture as a Path to Genomic Instability? *Trends Cell Biol.* 27:546–555. https://doi.org/10.1016/j.tcb.2017.02.008

Spektor, A., N.T. Umbreit, and D. Pellman. 2017. Cell Biology: When Your Own Chromosomes Act like Foreign DNA. *Curr. Biol.* 27:R1228–R1231. https://doi.org/10.1016/j.cub.2017.09.043

Stukey, J.E., V.M. McDonough, and C.E. Martin. 1989. Isolation and characterization of OLE1, a gene affecting fatty acid desaturation from Saccharomyces cerevisiae. *J. Biol. Chem.* 264:16537–16544.

Tatzer, V., G. Zellnig, S.D. Kohlwein, and R. Schneiter. 2002. Lipid-dependent subcellular relocalization of the acyl chain desaturase in yeast. *Mol. Biol. Cell.* 13:4429–4442. https://doi.org/10.1091/mbc.e02-04-0196

Teis, D., S. Saksena, and S.D. Emr. 2008. Ordered assembly of the ESCRT-III complex on endosomes is required to sequester cargo during MVB formation. *Dev. Cell.* 15:578–589. https://doi.org/10.1016/j.devcel.2008.08.013

Thaller, D.J., M. Allegretti, S. Borah, P. Ronchi, M. Beck, and C.P. Lusk. 2019. An ESCRT-LEM protein surveillance system is poised to directly monitor the nuclear envelope and nuclear transport system. *eLife.* 8: e45284. https://doi.org/10.7554/eLife.45284

Umbreit, N.T., and D. Pellman. 2017. Cancer biology: Genome jail-break triggers lockdown. *Nature.* 550:340–341. https://doi.org/10.1038/nature24146

Ungricht, R., and U. Kutay. 2017. Mechanisms and functions of nuclear envelope remodelling. *Nat. Rev. Mol. Cell Biol.* 18:229–245. https://doi.org/10.1038/nrm.2016.153

Vietri, M., K.O. Schink, C. Campsteijn, C.S. Wegner, S.W. Schultz, L. Christ, S.B. Thoresen, A. Brech, C. Raiborg, and H. Stenmark. 2015. Spastin and ESCRT-III coordinate mitotic spindle disassembly and nuclear envelope sealing. *Nature.* 522:231–235. https://doi.org/10.1038/nature14408

Vietri, M., S.W. Schultz, A. Bellanger, C.M. Jones, C. Raiborg, E. Skarpen, C.R.J. Pedurupillay, E. Kip, R. Timmer, A. Jain, et al. 2019. Unrestrained ESCRT-III drives chromosome fragmentation and micronuclear catastrophe. *bioRxiv*. 517011.

Wang, S., F.B. Romano, C.M. Field, T.J. Mitchison, and T.A. Rapoport. 2013. Multiple mechanisms determine ER network morphology during the cell cycle in Xenopus egg extracts. *J. Cell Biol.* 203:801–814. https://doi.org/10.1083/jcb.201308001

Watt, S., J. Mata, L. López-Maury, S. Marguerat, G. Burns, and J. Bähler. 2008. urg1: a uracil-regulatable promoter system for fission yeast with short induction and repression times. *PLoS One.* 3:e1428. https://doi.org/10.1371/journal.pone.0001428

Webster, B.M., D.J. Thaller, J. Jäger, S.E. Ochmann, S. Borah, and C.P. Lusk. 2016. Chm7 and Heh1 collaborate to link nuclear pore complex quality control with nuclear envelope sealing. *EMBO J.* 35:2447–2467. https://doi.org/10.15252/embj.201694574

Wollert, T., C. Wunder, J. Lippincott-Schwartz, and J.H. Hurley. 2009. Membrane scission by the ESCRT-III complex. *Nature.* 458:172–177. https://doi.org/10.1038/nature07836

Wu, J.Q., C.D. McCormick, and T.D. Pollard. 2008. Chapter 9: Counting proteins in living cells by quantitative fluorescence microscopy with internal standards. *Methods Cell Biol.* 89:253–273. https://doi.org/10.1016/S0091-679X(08)00609-2

Yam, C., Y. He, D. Zhang, K.H. Chiam, and S. Oliferenko. 2011. Divergent strategies for controlling the nuclear membrane satisfy geometric constraints during nuclear division. *Curr. Biol.* 21:1314–1319. https://doi.org/10.1016/j.cub.2011.06.052

Supplemental material

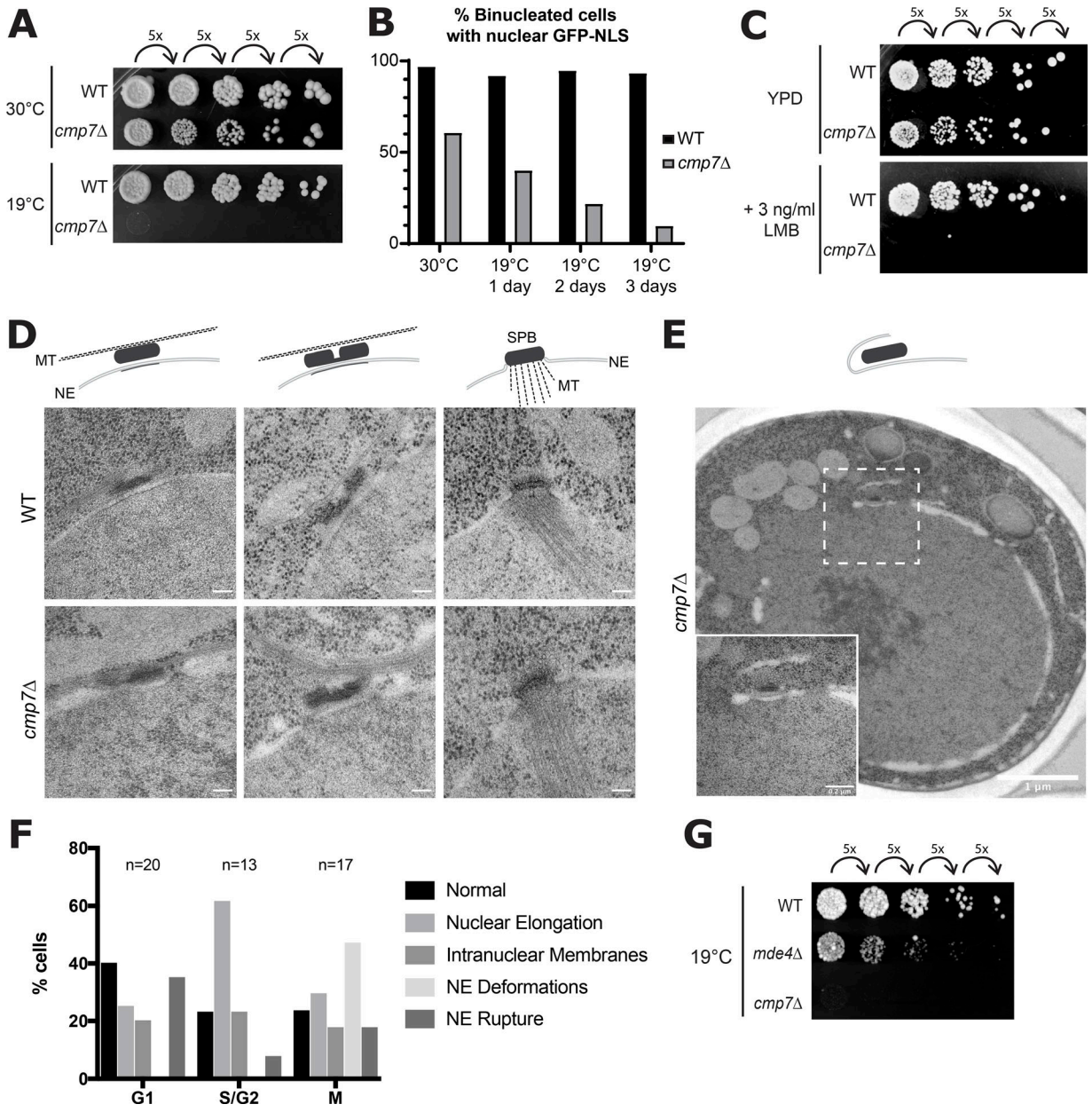

Figure S1. **Accentuation of the nuclear envelope integrity defect of *cmp7Δ* cells at 19°C. (A)** Growth of WT and *cmp7Δ* cells at 30°C for 3 d as compared with growth at 19°C for 7 d. **(B)** Percentage of WT or *cmp7Δ* binucleated cells with nuclear GFP-NLS in both daughters at 30°C and 19°C. *n* = 69–257. **(C)** Growth of WT and *cmp7Δ* cells on YPD or YPD with 3 ng/ml LMB at 30°C for 3 d. **(D and E)** Serial section EM was used to reconstruct full nuclei from WT and *cmp7Δ* cells grown at 19°C. **(D)** Example images of normal-appearing unduplicated and duplicated side-by-side SPBs, which are located on the cytoplasmic face of the NE as illustrated in the schematic. In mitosis, SPBs are inserted into the NE. MT, microtubules. Scale bars, 100 nm. **(E)** Example image of a *cmp7Δ* cell with ruptured NE adjacent to SPB (as shown in inset). Scale bar, 1 µm. Scale bar in the inset, 0.2 µm. **(F)** The frequency of the above phenotypes during the cell cycle determined based on SPB duplication state and microtubule morphology. G1 cells, single unduplicated SPB; S/G2 cells, duplicated SPBs; and M cells, nuclear microtubules. The total number of cells is shown. **(G)** *mde4Δ* is not as cold-sensitive as *cmp7Δ*.

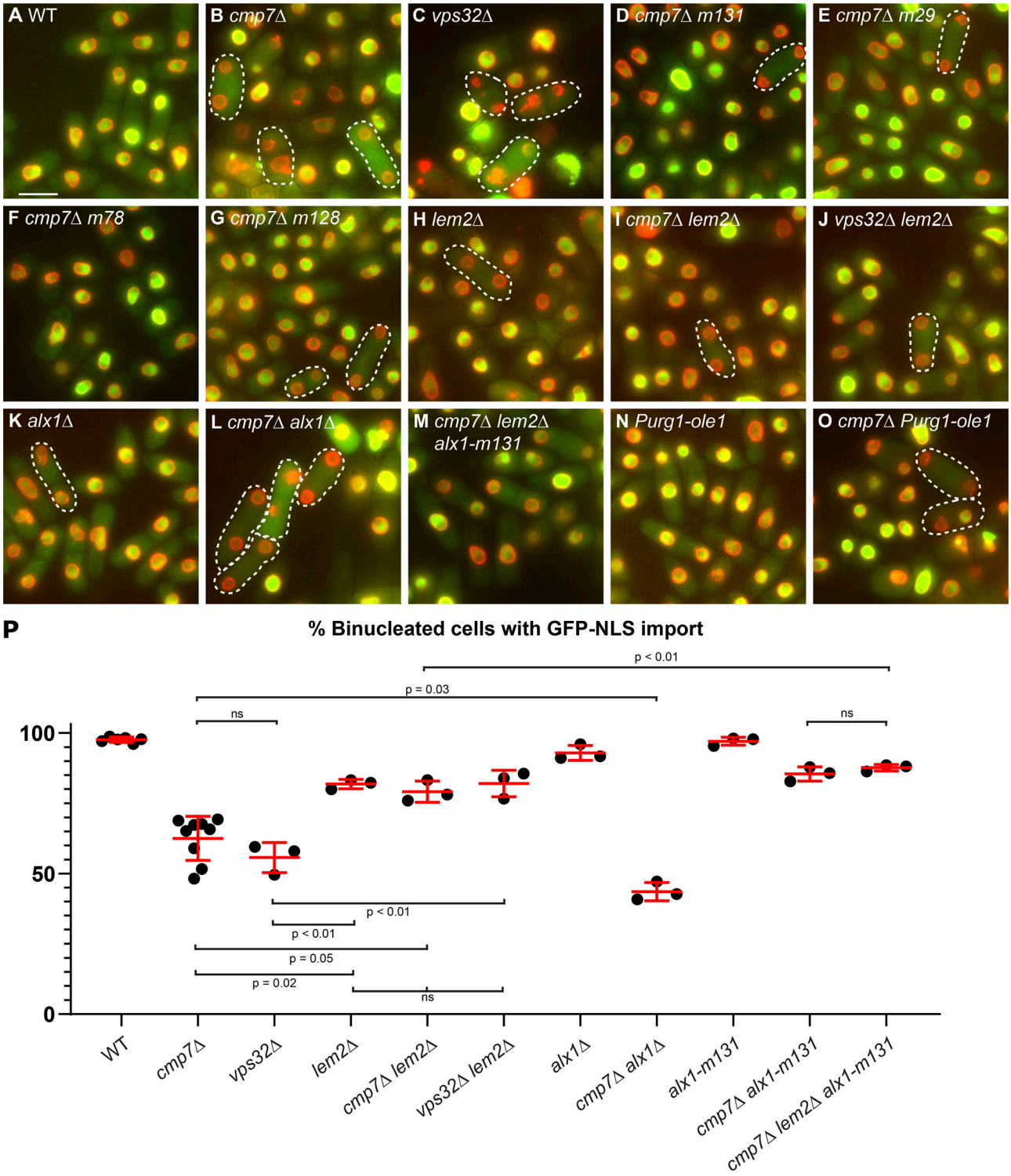

Figure S2. **Representative images of various mutants expressing GFP-NLS (green) Nup85-mCherry (red) cultured at 30°C.** Maximum intensity projections of five z-slices near the middle of the cells were shown. Binucleated cells with no nuclear GFP-NLS in either daughter nuclei or with nuclear GFP-NLS in only one daughter nucleus were indicated by white dashed lines. Scale bar, 10 µm. **(A)** WT. **(B)** *cmp7Δ*. **(C)** *vps32Δ*. **(D)** *cmp7Δ m131*. **(E)** *cmp7Δ m29*. **(F)** *cmp7Δ m78*. **(G)** *cmp7Δ m128*. **(H)** *lem2Δ*. **(I)** *cmp7Δ lem2Δ*. **(J)** *vps32Δ lem2Δ*. **(K)** *alx1Δ*. **(L)** *cmp7Δ alx1Δ*. **(M)** *alx1-m131 cmp7Δ lem2Δ*. **(N)** *Purg1-ole1*. **(O)** *cmp7Δ Purg1-ole1*. **(P)** Percentage of binucleated cells with nuclear GFP-NLS in both daughters at 30°C. Mean ± SD from three experiments is shown. *n* = 83–424 per strain in each experiment.

Tables S1 and S2 are provided online. Table S1 lists bypass suppressors of *cmp7*Δ identified in this study. Table S2 lists *S. japonicus* strains used in this study.